

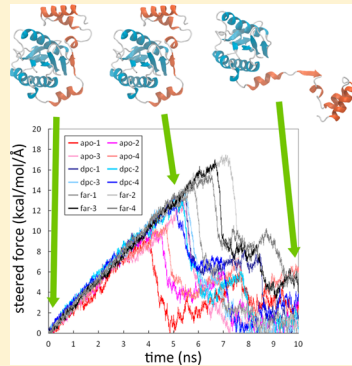
Lipid Regulated Conformational Dynamics of the Longin SNARE Protein Ykt6 Revealed by Molecular Dynamics Simulations

Jingwei Weng,[†] Yanhong Yang,[†] and Wenning Wang*,^{†,‡}

[†]Shanghai Key Laboratory of Molecular Catalysis and Innovative Materials, Department of Chemistry, and [‡]Institutes of Biomedical Sciences, Fudan University, Shanghai 200433, P.R. China

Supporting Information

ABSTRACT: The conformation and subcellular localization of R-SNARE protein Ykt6 are regulated by the lipidation state of its C-terminal CCAIM motif. Biochemical and crystallography studies showed that lipid molecules binding at a hydrophobic pocket at the interface between the longin domain and the SNARE core can lock Ykt6 at a closed conformation and mimic the farnesylated state of Ykt6. In this study, we performed *in silico* farnesylation of Ykt6 and explored the conformational dynamics of Ykt6 using conventional and steered MD simulations. We found that the farnesylated Ykt6 model structure is stable during the 2 μ s simulation and the farnesyl group adopts conformations similar to those of the DPC molecule bound to Ykt6. Both DPC binding and farnesylation were found to reduce the conformational flexibility of Ykt6 and hinder the dissociation of SNARE core from the longin domain. The dissociation of the α F- α G segment is the rate-limiting step during the putative closed-to-open conformational transition of Ykt6, and the key residues involved in this process are consistent with the experimental mutagenesis study.



1. INTRODUCTION

Membrane fusion is a fundamental biochemical reaction and the final step in all membrane trafficking events. The SNARE (soluble N-ethylmaleimide-sensitive factor attachment receptor) complex has a central position in the membrane fusion process.^{1–6} SNARE proteins can be classified into Q-SNAREs and R-SNAREs according to a conserved glutamine or arginine in the center of the SNARE core domain.^{7,8} In general, each SNARE protein comprises a central SNARE core domain of 60–70 amino acids, a variable N-terminal domain, and a C-terminal transmembrane anchor.⁵ The conserved SNARE core domain mediates the assembly of the four-helix bundle SNARE complex. The N-terminal domain plays an important role in modulating the SNARE function and shows sequential and structural diversities.⁹ The N-terminal H_{abc} domain of Q-SNARES consists of a three-helix bundle and can interact with the SNARE core domain to control its interaction with other SNAREs.^{10–13} For a subset of R-SNAREs, such as Ykt6, Sec22B, and VAMP7 in mammals, the N-terminal longin domain plays a similar role by interacting with the SNARE core domain and inhibiting its SNARE function.^{14–16}

Ykt6 is a longin domain SNARE protein first discovered in yeast as an R-SNARE involved in multiple transport steps between the Golgi and vacuole.^{17–19} In mammals, Ykt6 is highly enriched in brain neurons and has very low expression levels in other types of cells.²⁰ Although most SNAREs are permanently anchored to membranes by their C-terminal transmembrane segments, Ykt6 lacks a transmembrane domain for membrane anchoring.¹⁷ Instead, it is lipidated at a C-terminal conserved CCAIM motif, with the first cysteine palmitoylated and the second cysteine farnesylated.^{17,21} Ykt6 is found both on

intracellular membranes and in the cytosol. The single farnesylated Ykt6 was assumed to adopt a closed conformation and exist in cytosol, whereas the stable membrane association requires both farnesylation and palmitoylation at the CCAIM motif.^{20,21} The cytosolic form of Ykt6 is fusion-inactive due to the autoinhibition of the SNARE core by its N-terminal longin domain.¹⁶ Recently, the structure of the full-length rat Ykt6 in complex with a fatty acid (DPC, dodecylphosphocholine) was solved.²² In sharp contrast to the SNARE core motifs found in syntaxin SNAREs, the Ykt6 SNARE core forms four discontinuous helices that wrap around the longin domain, and together form a compact globular structure with dominantly closed conformation in solution (Figure 1A). The fatty acid chain of DPC, buried in a hydrophobic groove formed between the longin domain and the SNARE core, is essential for maintaining the closed and autoinhibited conformation of Ykt6.²² This Ykt6/lipid complex structure indicate that the conformational and functional dynamics of Ykt6 are likely controlled by the coordinated actions of the longin domain, the SNARE core, and the covalently attached lipids.

However, the detailed mechanism of lipid modulated conformational dynamics of Ykt6 remains elusive. First, does the Ykt6/DPC complex crystal structure well mimic the farnesylated Ykt6? How does lipid binding or lipidation stabilize the closed state of Ykt6? How does the SNARE core domain

Special Issue: 25th Austin Symposium on Molecular Structure and Dynamics

Received: July 28, 2014

Revised: September 29, 2014

Published: September 30, 2014

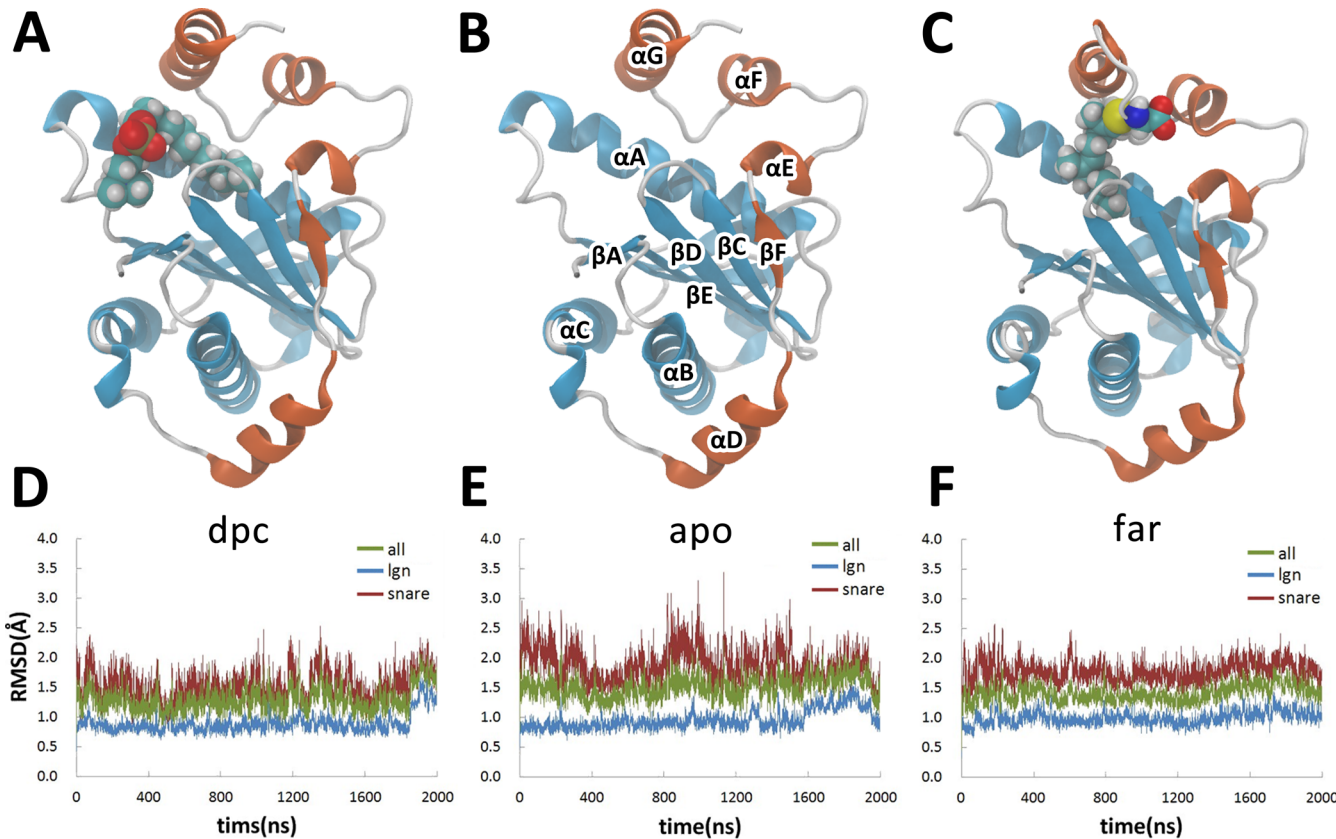


Figure 1. Overall conformational dynamics of Ykt6. (A) Crystal structure of the Ykt6/DPC complex. The longin and SNARE domains are brown and blue, respectively. The DPC molecule is shown with a space filling model. (B) Initial structure of the *apo* system obtained by removing DPC from the crystal structure. (C) Structure model of the *far* system. The farnesyl group is shown with a space filling model. (D) (E) (F) Time variations of the C_{α} -RMSD of *dpc*, *apo*, and *far* systems, respectively.

dissociate from the longin domain? In this study, we performed *in silico* farnesylation of Ykt6 and conducted 2 μ s long MD simulations to study how DPC binding and lipidation affect the structure and the dynamics of Ykt6 protein. Lipid-dependent local structural rearrangements were observed at the longin–SNARE interface, which stabilizes the autoinhibition structure of Ykt6. Steered MD simulation was also employed to elucidate the dissociation process of the SNARE core domain from the longin domain.

2. METHODS

2.1. Simulation Parameters. The conventional MD simulations were conducted by using the software ACEMD 1.2.²³ The protein and lipid were described by CHARMM27 force field,^{24,25} and the water molecules were represented by the TIP3P model.²⁶ The force field parameters of the farnesyl group were transferred from those of methionine and 1-palmitoyl-2-oleoylphosphatidylcholine (POPC).

Parallel simulations were performed for three Ykt6 systems to study the effect of lipid or lipidation on protein dynamics: Ykt6 in complex with a DPC molecule as shown in the crystal structure (denoted as *dpc* hereafter), Ykt6 with the DPC molecule removed (denoted as *apo* hereafter), and Ykt6 farnesylated at the C-terminal Cys195 (denoted as *far* hereafter). The crystal structure of Ykt6 was obtained from the protein data bank (PDB ID: 3KYQ). The farnesyl tail of the *far* system was first manually overlapped onto the hydrophobic tail of DPC and then optimized by HADDOCK^{27,28} as described in our previous work.²² The *apo* system was built by directly removing the DPC

molecule from the Ykt6/DPC complex structure. The protein was solvated in a water box and a few water molecules were replaced by Na^+ and Cl^- ions to raise the salt concentration to 0.15 mol/L. Titratable residues were assumed to stay in their standard protonation states. As an example of a typical system, there are totally ~48 000 atoms in the rectangular simulation box measured $\sim 80 \times 80 \times 80 \text{ \AA}^3$. The Langevin thermostat was employed to maintain the system at 300 K and the damping constant was set as 0.1/ps. Holonomic constraints were cast on all hydrogen-heavy atom bond terms and the mass of hydrogen atoms was scaled by a factor of 4, allowing a time step of 4 fs.²⁹ Nonbonded and electrostatic interactions were calculated at every time step. Electrostatic interactions were evaluated using the particle-mesh Ewald (PME) method³⁰ with a grid density of 1 \AA . VDW interactions were smoothed beyond 10 \AA and truncated at 12 \AA . The ionized system was energy-minimized by 3000 steps with the heavy atoms of the protein restrained, followed by a 120 ps equilibration run with the restraints on the protein gradually reduced. The production run lasted for 2 μ s with the system kept in the NVT ensemble and with all restraints removed. Coordinates were saved every 20 ps. Data analysis and molecular visualization were conducted by VMD.³¹ In the clustering analysis, a quality-threshold (QT) based algorithm was used.³²

2.3. Steered MD. Steered MD simulations were conducted by using the tclforce module of NAMD 2.8.³³ The constant-velocity protocol was employed and the potential applied to the protein can be written as

$$U = \frac{1}{2}k[d(t) - d^*(t)]^2 \quad (1)$$

in which k is the force constant, $d(t)$ is the instantaneous distance between the mass centers of the selected atom groups, and $d^*(t)$ is the preset distance. For the CM mode, in which the longin domain and the SNARE core domain are defined as the steered groups, respectively, the steer force is evenly distributed on the C_α atoms of each domain. The force constant is set to 1 (kcal/mol)/ \AA^2 and $d^*(t)$ is set to increase by 3 $\text{\AA}/\text{ns}$. Four independent trajectories with different initial velocities were produced for each system and each trajectory lasting for 10 ns. The mass of hydrogen atoms was set to the normal value and the time step was 1 fs. In the CN mode, the steer forces were applied on the N and C terminal residues of Ykt6 (Glu1 and Arg191), respectively. The force constant was 1 (kcal/mol)/ \AA^2 , whereas $d^*(t)$ was set to increase by 10 $\text{\AA}/\text{ns}$.

3. RESULTS

3.1. Overall Conformational Dynamics of Ykt6. The C_α root-mean-square deviation (RMSD) profiles of the entire protein with respect to the initial structure show that all three systems are generally stable throughout the 2 μs simulations (Figure 1D–F). The C_α RMSDs of the protein as a whole are larger than those of the longin domain (Figure 1D–F). It is not surprising, because the longin domain was previously shown to be well folded alone¹⁶ and has lower B factors in the crystal structure of the full length Ykt6.²² The C_α RMSDs of the SNARE core are larger than those of the whole protein in all three systems (Figure 1D–F), showing that the SNARE core part has higher conformational flexibility. This is also consistent with the fact that the B factors of the SNARE core are relatively higher than the other regions of the protein in the crystal structure of full length Ykt6.²² The average RMSDs of the three systems show that the structural deviations of the **dpc** system are the smallest whereas that of the **apo** system is the largest (Table 1). It is

Table 1. Average C_α RMSDs of the Whole Protein and the Individual Domains of Ykt6

	average RMSD (\AA)		
	all	longin	snare
dpc	1.29(0.22)	0.89(0.17)	1.50(0.28)
apo	1.50(0.21)	0.97(0.18)	1.85(0.30)
far	1.41(0.15)	1.00(0.12)	1.78(0.18)

noteworthy that the overall structure of the farnesylated Ykt6 is quite stable throughout the 2 μs simulations, implying the reliability of the structure model of the **far** system built on the basis of the crystal structure of the DPC-bound Ykt6.²²

To investigate the feature of the conformational movement of Ykt6, we performed principle component analyses (PCA) for the simulation trajectory of the **apo** system. The first eigenvector is dominated by the motions at the C terminal region of the protein, especially the αG helix, whereas the second eigenvector is mainly the fluctuation of αD helix. These regions are all flexible in the protein as shown by the C_α RMSDs (Figure 1D–F) and RMSFs (Figure S1, Supporting Information). To compare the conformational spaces sampled by the three systems, we projected all the trajectories onto the first two PCA eigenvectors of the **apo** system (Figure 2). These two modes contribute 18.0% and 11.3% to the total motions respectively and are dominated by motions of the SNARE core domain, especially αD and αG

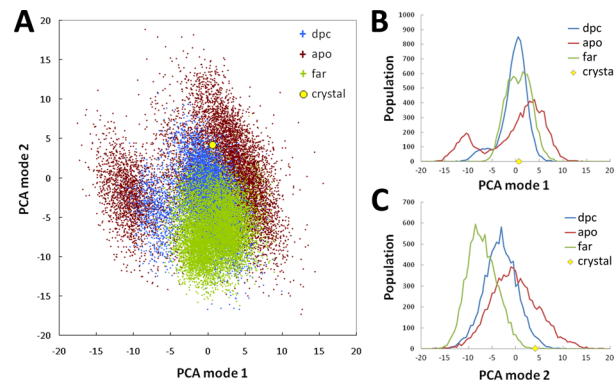


Figure 2. Conformational spaces of the three Ykt6 systems. (A) Projection of the simulation trajectories onto the 2D conformational space spanned by the first two PCA modes of the **apo** Ykt6. The trajectories of the **apo**, **dpc**, and **far** systems are shown as red, blue, and green dots, respectively. The position of the crystal structure is indicated by the yellow sphere. (B) (C) Projection of the simulation trajectories onto the first and second PCA modes, respectively. The position of the crystal structure is indicated by the yellow diamond.

helices (Figure S2, Supporting Information). It is shown that the **apo** system obviously samples larger conformational space than the **dpc** and the **far** systems do (Figure 2). Along the first PCA mode, the **apo** system obviously has two conformational states, whereas the **dpc** and **far** systems have much narrower distributions (Figure 2B). Therefore, lipid binding or lipidation effectively restricts the conformational movements of Ykt6. It is worth noting that the conformational space of the **apo** system generally covers those of the **dpc** and **far** systems, indicating that the conformational changes of Ykt6 upon lipid binding or farnesylation likely follow the “conformational selection” mechanism.

3.2. Conformational Changes of the Lipid-Binding Pocket Induced by the Protein–Lipid Interactions. As the DPC or farnesyl group binds to a hydrophobic pocket surrounded by αA , βC , βD , αE , αF , and αG , the lipidation state might directly affect the conformation of this pocket. To characterize the conformational changes upon lipid binding, we examined some inter-residue distances inside this hydrophobic pocket. Using αA helix as a reference point, the relative positions of the other secondary structure segments are measured by inter-residue distances (Figure 3A). The inter-residue distance between Met40 and Phe184 (denoted as D_{40-184}) was used to characterize the position of αG relative to αA helix (Figure 3A). The distribution of D_{40-184} in both **dpc** and **far** systems center around 12.4 \AA , shorter than that of the crystal structure (13.1 \AA). The **apo** system, however, has a bimodal distribution of D_{40-184} with the higher peak at a longer distance (13.6 \AA) and the lower peak at a distance similar to that in **dpc** and **far** systems (Figure 3B). The variation of D_{40-184} along the simulation trajectory shows that the distance switched between the longer and shorter values frequently (Figure S3, Supporting Information), indicating that this part of the binding pocket is flexible in the **apo** state. On the other hand, the DPC molecule interacts with αG (section 3.3) and the farnesyl group is covalently linked to αG . These may all restrain the D_{40-184} distance. The distance between Met40 and Thr64 (D_{40-64} , Figure 3A,C), which measures the relative positions of αA and βD , also shows differences among the three systems. D_{40-64} of **apo** system is obviously shorter than those of the **dpc** and **far** systems. On the other hand, the positions of αE or αF relative to αA do not show obvious differences among the

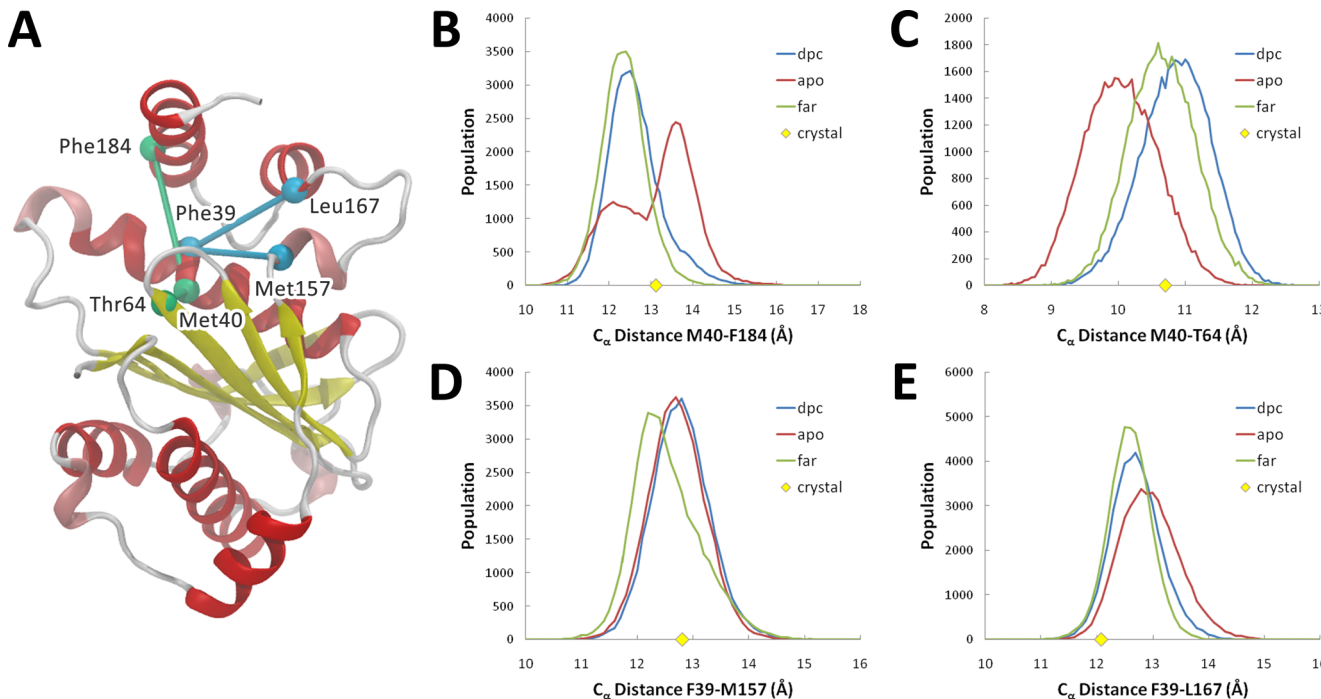


Figure 3. Conformational changes of the lipid-binding pocket. (A) Inter-residue distances that measure the conformational changes of the lipid-binding pocket. The distances are shown as sticks connecting the C_{α} atoms of the two residues, which are rendered as colored balls. (B) Distributions of the D_{40-184} distances in the three Ykt6 systems. (C) Distributions of the D_{40-64} distances in the three Ykt6 systems. (D) Distributions of the D_{39-157} distances in the three Ykt6 systems. (E) Distributions of the D_{39-167} distances in the three Ykt6 systems. The corresponding distances in the crystal structure are indicated by the yellow diamonds.

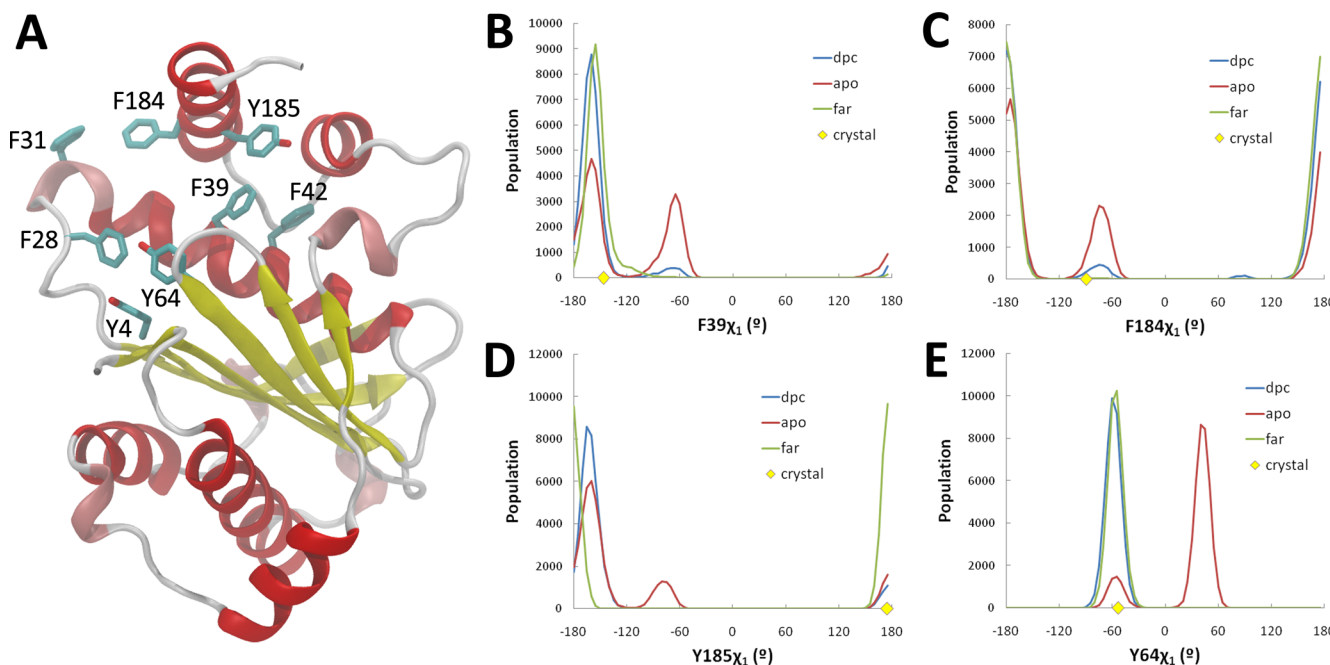


Figure 4. Side chain orientations of residues inside the lipid-binding pocket. (A) Some aromatic residues inside the lipid-binding pocket. The side chains of the aromatic residues are shown with the stick model. (B) χ_1 angle distributions of Phe39 in the three Ykt6 systems. (C) χ_1 angle distributions of Phe184 in the three Ykt6 systems. (D) χ_1 angle distributions of Tyr185 in the three Ykt6 systems. (E) χ_1 angle distributions of Tyr64 in the three Ykt6 systems. The corresponding angles in the crystal structure are indicated by the yellow diamonds.

three systems. The shifts of D_{39-157} and D_{39-167} are less than 0.2 Å (Figure 3D,E), indicating that these segments are less sensitive to lipid interaction.

Compared to the backbone fluctuations, the side chain orientation is more sensitive to lipid binding. To characterize

these variations, we measured the side chain dihedral angle χ_1 of all the aromatic residues in proximity to DPC in the crystal structure (Figure 4A). Comparison of the χ_1 distributions in the three systems clearly shows that some of the aromatic residues, including Phe39 on α A, Tyr64 on β D, and Phe184 and Tyr185

on α G, have at least two side chain orientation states in the **apo** system whereas lipid binding confines the side chain orientation to one of the states (Figure 4B–E). For example, χ_1 of Phe39 in the **apo** system has two comparable populations at -155° and -65° (Figure 4B), whereas in the **dpc** and **far** systems most of the populations center at $\chi_1 = -155^\circ$, which is similar to the crystal structure ($\chi_1 = -146^\circ$). For Phe184 and Tyr185, lipid binding shifts the populations to the major states with χ_1 centered at -175° and -165° , respectively (Figure 4C,D). For Tyr64, interestingly, the major side chain orientation is $\chi_1 = 40^\circ$ in the **apo** system, whereas lipid binding switches the orientation completely to the minor state of **apo** system with $\chi_1 = -60^\circ$ (Figure 4E), indicating that the side chain of Tyr64 adopts totally different orientations upon lipid binding. On the other hand, residues at the periphery of the binding pocket are all insensitive to lipid binding. The χ_1 distributions of the phenylalanines on the β B- α A loop (Phe28 and Phe31) and on α A helix (Phe42) and the tyrosine on the β A strand (Phe4) were hardly disturbed by lipid binding (Figure S4, Supporting Information). Taken together, lipid binding was found to decrease the side chain flexibility of the residues inside the hydrophobic pocket, and DPC and the farnesyl group have effects very similar to those of the residue side chains.

The buried surface area (BSA) between the longin and the SNARE core domains was evaluated to further characterize the lipid binding pocket (Table 2). Taking the DPC/farnesyl group

Table 2. Average Buried Surface Areas (BSAs) between the Longin Domain and the SNARE Core Domain of the Three Ykt6 Systems over the last 0.5 μ s

interface	BSA (\AA^2)		
	apo	dpc	far
longin SNARE+lipid ^a		1712 \pm 45	1615 \pm 45
longin-SNARE ^b	1349 \pm 66	1504 \pm 61	1390 \pm 44
longin-lipid		342 \pm 8	329 \pm 19
longin- α F α G	488 \pm 50	615 \pm 57	476 \pm 25
longin- α D α E β F	707 \pm 36	751 \pm 29	719 \pm 38
longin- α D	332 \pm 35	357 \pm 21	317 \pm 33
longin- α E	313 \pm 24	325 \pm 24	337 \pm 23
longin- β F	226 \pm 17	243 \pm 18	229 \pm 14

^aBSA between SNARE core plus lipid (or farnesyl group) and the longin domain. ^bThe hydrophobic tail of the farnesyl group was excluded in BSA calculation.

as a part of the SNARE core domain, the BSA between longin and SNARE cores in the **dpc** and the **far** systems are 1695 and 1616 \AA^2 , respectively, which are significantly larger than that in the **apo** system (1361 \AA^2) (Table 2). When DPC is excluded, the BSA between longin and SNARE core domains in the **dpc** system is still larger than that of the **apo** system by 126 \AA^2 (Table 2), whereas the BSA of the **far** system excluding the farnesyl group is only slightly larger than that of the **apo** system (Table 2). Therefore, DPC can significantly enhance the packing between longin and SNARE domains. The enhanced packing in the **dpc** system is most evident between the C terminal α F- α G segment and the longin domain, the BSA of which is larger than that of **apo** system by 104 \AA^2 (Table 2). Compared to the **dpc** system, the **far** system is relatively loosely packed. The increased BSA with respect to the **apo** system is mainly contributed by the farnesyl group *per se*, whereas the packing between the longin and SNARE core is similar to that in the **apo** system. Taken together, the BSA calculation is quite consistent with the above inter-

residue distance analysis of the hydrophobic pocket, showing that the presence of **dpc** well stabilizes the hydrophobic groove and substantially strengthens the longin-SNARE interface.

3.3. Intrinsic Flexibility of DPC and the Farnesyl Group inside the Hydrophobic Groove. Although DPC closely associated with Ykt6 throughout the simulation, the lipid exhibited conformational flexibility inside the binding pocket. Cluster analysis of DPC conformations in the simulation gives four clusters with populations larger than 10% (Table S1). In the largest cluster (cluster 1) with over 40% populations, the DPC molecule adopts a conformation similar to that in the crystal structure (Figure 5A). The polar headgroup of DPC points

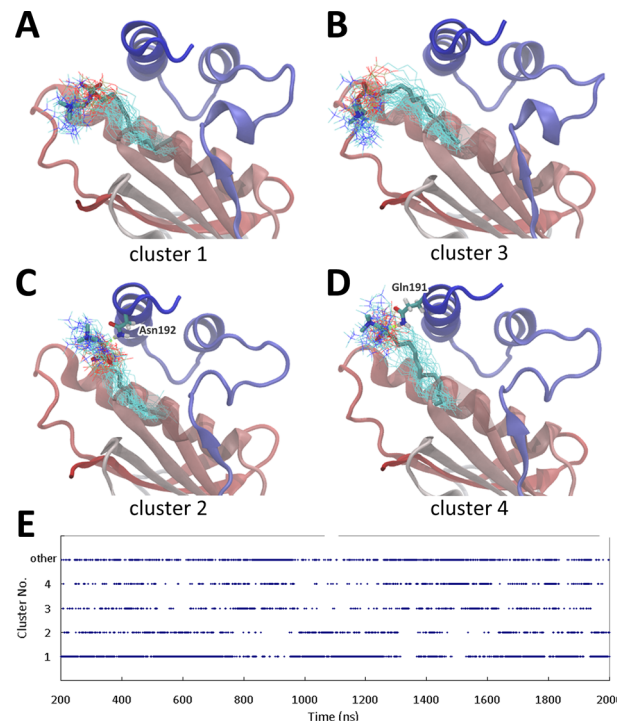


Figure 5. Conformations of DPC in the lipid-binding pocket. (A) Conformations of cluster 1 in the clustering analyses of the DPC molecule. The protein is represented by ribbons. The lipid is colored by the atom type (cyan for carbon, blue for nitrogen, red for oxygen, and gold for phosphor) and is drawn as licorice for the center structure and as lines for some other structures in the cluster. For clarity, the β C- β D loop is made transparent. (B) Conformations of cluster 3. (C) Conformations of cluster 2. (D) Conformations of cluster 4. The hydrogen bond formed between DPC and Ykt6 is denoted as a green dotted line. (E) Populations among the largest four clusters of DPC along the simulation trajectory.

toward the N terminus of the protein and the aliphatic tail inserts into the hydrophobic pocket (Figure 5A). The DPC conformation in cluster 3 is similar to that of cluster 1, but the aliphatic tail does not insert into the pocket as deep as in cluster 1 (Figure 5B). Clusters 2 and 4 represent the second type of the DPC conformation, in which the polar headgroup points upward and gets closer to the C-terminal α G helix (Figure 5C,D). By approaching the C-terminal α G helix, the phosphor group of DPC in cluster 2 or 4 forms hydrogen bonds with the polar residues on α G, such as Gln191 and Asn192 (Figure 5C,D). Therefore, these hydrogen bond interactions might be the main driving force that pulls the polar headgroup of DPC toward the C-terminus in clusters 2 and 4. Along the simulation trajectory, the DPC conformation switched frequently among various

clusters (Figure 5E), indicating the high conformational flexibility of the polar headgroup. This is also consistent with the fact that the electron density of the DPC molecule in the crystal structure is weak and discontinuous.²²

We also performed cluster analysis of the farnesyl group in the **far** system. The largest cluster has a population over 60%, in which the aliphatic tail of the farnesyl group inserts into the hydrophobic pocket in a fashion similar to DPC (Figure 6A).

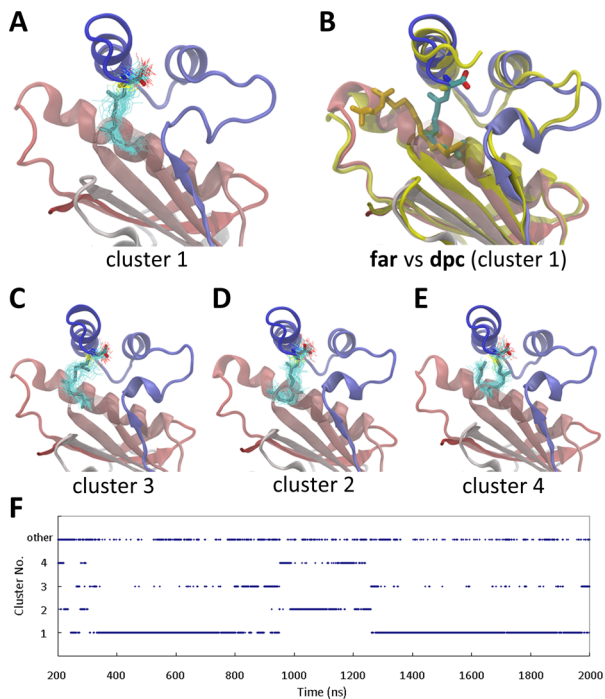


Figure 6. Conformations of the farnesyl group in the lipid-binding pocket. (A) Conformations of cluster 1 in the clustering analyses of farnesyl group. The protein is represented by ribbons. The lipid is colored by the atom type (cyan for carbon, blue for nitrogen, red for oxygen, and gold for phosphorus) and is drawn as licorice for the center structure and as lines for some other structures in the cluster. For clarity, the $\beta\text{C}-\beta\text{D}$ loop is made transparent. (B) Superimposition of cluster 1 conformations of the **dpc** and **far** systems. (C) Conformations of cluster 3. (D) Conformations of cluster 2. (E) Conformations of cluster 4. (F) Populations among the largest four clusters of the farnesyl group along the simulation trajectory.

Superimposition of the **far** and **dpc** systems shows that the aliphatic tail of farnesyl group perfectly overlaps with the tail of DPC in cluster 1 (Figure 6B). The farnesyl group conformation of cluster 3 is similar to that of cluster 1, with slightly different insertion depth of the aliphatic tail (Figure 6C). The farnesyl group can also adopt other conformations as shown in clusters 2 and 4, in which the aliphatic tail reoriented to interact with the other hydrophobic residues inside the binding pocket (Figure 6D,E). Different from DPC, the conformational flexibility of the farnesyl group is mainly manifested on the aliphatic tail and the simulation results show that the hydrophobic pocket can well accommodate various conformations of the farnesyl group (Figure 6). The conformational changes of the farnesyl group, however, are much less frequent than those of DPC (Figure 6F). Especially, the switch between the cluster 1 conformation and cluster 2/4 conformations is very slow (Figure 6F), showing that the aliphatic tail of the farnesyl group is quite stable.

3.4. Lipid Binding or Lipidation Hinders the Longin–SNARE Core Dissociation. The intramolecular interaction between the longin domain and the SNARE core must be disrupted to form the SNARE complex. To examine the effect of lipidation on the longin–SNARE core dissociation, we performed steered MD simulations to explore the dissociation processes in the **apo**, **dpc**, and **far** systems. The steer forces were applied on the centers of mass of the longin domain and the SNARE core, respectively (referred to CM mode hereafter), and the constant speed steered MD method was used. Four independent trajectories of 10 ns long were conducted for each system. Multicopy simulations gave consistent results, revealing generally similar features of the dissociation process among various trajectories as well as the three systems (see below for more details). However, the easiness of the dissociation of the SNARE core from the longin domain is obviously different among the three systems. The profiles of the steer forces along the simulation trajectories show that the forces applied on the **apo** system are the smallest (Figure 7A, Table S2, Supporting

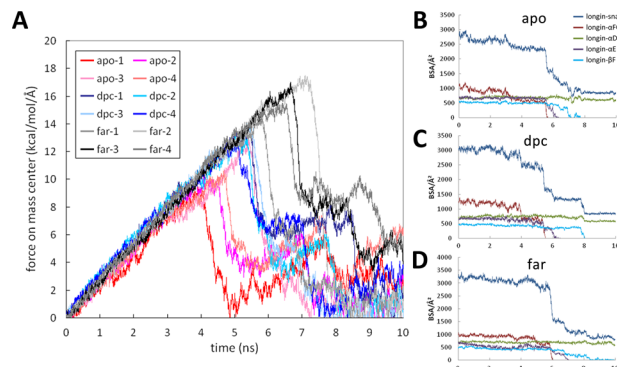


Figure 7. Closed-to-open transition of Ykt6 revealed by steered MD simulations. (A) Steer forces along the simulation trajectories of the three systems. (B) Variations of the BSA between the longin domain and various parts of the SNARE core along the simulation trajectories of the **apo** system. (C) Variations of the BSA between the longin domain and various parts of the SNARE core along the simulation trajectories of the **dpc** system. (D) Variations of the BSA between the longin domain and various parts of the SNARE core along the simulation trajectories of the **far** system.

Information). The maximal forces of the four independent trajectories range from 9.5 to 12.9 (kcal/mol)/ \AA^2 (Table S2, Supporting Information). For the **dpc** system, the maximal forces range from 12.8 to 14.0 (kcal/mol)/ \AA^2 . The **far** system requires the largest steer forces, ranging from 14.5 to 17.5 (kcal/mol)/ \AA^2 (Table S2 (Supporting Information), Figure 7A). Therefore, lipid binding or lipidation makes the longin–SNARE dissociation more difficult. It is interesting to note that the farnesylation Ykt6 has the most stable intramolecular interactions.

The BSA values between the longin and the SNARE core were used as a probe for monitoring the disruption of the intramolecular interactions. The times of the appearance of the maximal forces in all the trajectories correspond to the dissociation of the $\alpha\text{F}-\alpha\text{G}$ segment from the longin domain, characterized by the abrupt decrease of the BSA (Figure 7B–D). Therefore, the interaction between the $\alpha\text{F}-\alpha\text{G}$ segment and the longin domain contribute most to the stability of the closed conformation. In the stage of the $\alpha\text{F}-\alpha\text{G}$ dissociation, hydrophobic interactions between αA and $\alpha\text{F}-\alpha\text{G}$ were disrupted, involving hydrophobic residues Phe39, Phe42,

Leu46, Leu170, Val171, Val176, Leu177, and Tyr185. Hydrogen bond interactions Glu38–Ser181, Glu38–Gly178 on α A and α F– α G, Arg88–Asp147, Thr92–Gln143 on α B and α D, and Glu61–Met157, Glu61–Met157 on α B and α E were also disrupted. In the **apo** system, the four simulation trajectories showed that the dissociation of the α F– α G segment from the longin domain took place between 4 and 6 ns (Figure 7B), which is the first step of the dissociation process. Subsequently, α E dissociated from the longin domain (Figure 7B). In three of the four trajectories, dissociation of β F was not observed at the end of the simulations (Figure S5, Supporting Information), but in one of the trajectories, β F dissociated from the longin domain shortly after the α E dissociation (Figure 7B). The time series of the steer force reflected the feature of a three-stage dissociation process. Three peaks of the steer force can be identified corresponding to the three dissociation stages, and the largest force appeared at the stage of α F– α G dissociation (Figure 7A), demonstrating that α F– α G dissociation is the rate-limiting step of the longin–SNARE core dissociation process. The second stage of α E dissociation involves disruption of many hydrophobic interactions among residues Leu46, Ile47, Val59, Leu65, Leu153, Met157, Leu160, and Leu161. In the third stage of β F dissociation, hydrogen bonds Ser58–His154, Lys60–His154 between β C and β F, and Arg50–Glu165 between α A and α F were broken. It is worth noting that during the steered MD simulations the structure of the longin domain is stable. The steer force did not disturb the structure integrity of the longin domain.

The steered MD simulations of the **dpc** and the **far** systems revealed similar features of longin–SNARE core dissociation. There is also a three-stage dissociation process (Figure 7C,D). However, the dissociation processes were obviously delayed in the **dpc** and **far** systems, consistent with the larger steer forces with respect to the **apo** system (Figure 7A). The abrupt BSA decrease due to α F– α G dissociation occurred around 5.5 ns in the **dpc** system and between 6 and 8 ns in the **far** system (Figure 7C,D). The delay implies that longin–SNARE core dissociation is more difficult. Therefore, comparison of the BSA profiles of the three systems shows that the longin–SNARE core dissociation is the easiest in the **apo** system and the most difficult in the **far** system.

To further verify the longin domain stability and examine the effect of steer force, we performed additional steered MD simulations of the **apo** system by exerting the steer forces on the N and C terminal residues of Ykt6, respectively (referred to as the CN mode). The resulting trajectories showed that the longin domain is also very stable throughout the simulations. The profiles of the BSAs along the trajectories do not exhibit an abrupt decrease, as shown in the MC mode simulation (Figure S6, Supporting Information). However, the three-stage dissociation feature is conserved, in which the dissociation process is initiated from the α F– α G segment (Figure S6, Supporting Information). Therefore, the results from the two simulation modes are consistent.

4. DISCUSSION

In this study, we explored the effect of lipid binding and lipidation on the conformational dynamics of the longin SNARE Ykt6 by MD simulations. During the 2 μ s simulations, different conformational dynamics of the three systems can be identified. The **apo** system exhibits higher conformational flexibilities than the DPC bound and farnesylated systems, and samples larger conformational spaces. This is in agreement with the experimental observations, showing that the full length **apo**

Ykt6 has multiple conformational states in solution.²² However, the **apo** system is expected to undergo much larger conformational changes than those observed in the MD simulations, such as the dissociation of the SNARE core from the longin domain. It is likely that the simulation time is limited, whereas the time scale for the conformation exchanges of the **apo** system is much longer. In the NMR ¹⁵N-HSQC spectrum of apo Ykt6, the split peaks indicate the slow exchanges of a millisecond time scale.²²

The overall conformation of the **far** system is very stable throughout the simulation, suggesting that the model structure built on the basis of the Ykt6/DPC complex may reasonably represent the farnesylated Ykt6. The fatty acid chain adopts similar conformations inside the hydrophobic binding pocket as the DPC molecule does. However, the farnesyl group exhibits less frequent conformational fluctuations than DPC does, probably due to its covalent linking to the C-terminus of the protein. Consistently, the steered MD simulations reveal that the SNARE-longin separation is more difficult in the farnesylated Ykt6 than that in the DPC bound one. Therefore, the closed conformation of the farnesylated Ykt6 should be more stable than that of the Ykt6/DPC complex. The steered MD simulations also verify that the structure of the longin domain remains stable during the SNARE core dissociation. It has been found that the dissociation of the α F– α G segment is likely the rate-limiting step during the closed-to-open conformational transition in Ykt6. Some key residues for SNARE-longin interactions, such as Phe39, Phe42, Val171, and Tyr185 identified in the steered MD simulations were also shown to affect the cell localization of Ykt6 in the mutagenesis experiments.³⁴ The closed conformation of Ykt6 is proposed to be opened upon palmitoylation mediated membrane insertion. How palmitoylation and membrane association disrupt the intramolecular interaction between SNARE core and longin domain remains unknown. Further biophysical and simulation studies are required to reveal this mystery.

5. CONCLUSIONS

The lipid modulated conformational dynamics of longin SNARE protein Ykt6 was studied by conventional MD and steered MD simulations. DPC binding and farnesylation were found to reduce the conformational flexibilities of Ykt6, especially those of the SNARE core domain of Ykt6. The farnesyl group was shown to adopt similar conformations in the lipid binding pocket as DPC does. The steered MD simulations demonstrated that DPC binding and farnesylation hinder the longin–SNARE dissociation and revealed the key step of the dissociation to be the displacement of the α F– α G fragment from the longin domain.

■ ASSOCIATED CONTENT

S Supporting Information

A table of clustering analyses of the conformations of the DPC and the farnesyl group, a table of the maximal forces, the occurrence times of the maximal forces, and the dissociation times of α F– α G segment in the steered MD trajectories of the three Ykt6 systems, a figure of the $C\alpha$ root mean square fluctuations (RMSF) of **apo**, **dpc**, and **far** Ykt6 systems during the 2 μ s simulations, a figure of the first two PCA modes, a figure of the time variations of the D_{40-184} distance in the **apo** system, a figure of the side chain orientations of some aromatic residues in the lipid binding pocket, a figure of the variations of the BSA between the longin domain and various parts of the SNARE core along the four CM mode steered MD simulation trajectories of the **apo** system, a figure of the variations of the BSA between the

longin domain and various parts of the SNARE core along the four CN mode steered MD simulation trajectories of the apo system. This material is available free of charge via the Internet at <http://pubs.acs.org>

AUTHOR INFORMATION

Corresponding Author

*W. Wang. Tel: +86-21-65643985; E-mail: wnwang@fudan.edu.cn.

Notes

The authors declare no competing financial interest.

ACKNOWLEDGMENTS

This work was supported by National Major Basic Research Program of China (2011CB808505, 2014CB910201), National Science Foundation of China (31070642, 21473034, B030204), Specialized Research Fund for the Doctoral Program of Higher Education (20130071140004), Science & Technology Commission of Shanghai Municipality (08DZ2270500). We thank the supercomputer center of Fudan University for their allocation of computer time.

REFERENCES

- (1) Sollner, T.; Whiteheart, S. W.; Brunner, M.; Erdjument-Bromage, H.; Geromanos, S.; Tempst, P.; Rothman, J. E. SNAP receptors implicated in vesicle targeting and fusion. *Nature* **1993**, *362*, 318–324.
- (2) McNew, J. A.; Parlati, F.; Fukuda, R.; Johnston, R. J.; Paz, K.; Paumet, F.; Sollner, T. H.; Rothman, J. E. Compartmental specificity of cellular membrane fusion encoded in SNARE proteins. *Nature* **2000**, *407*, 153–159.
- (3) Hu, C.; Ahmed, M.; Melia, T. J.; Sollner, T. H.; Mayer, T.; Rothman, J. E. Fusion of cells by flipped SNAREs. *Science* **2003**, *300*, 1745–1749.
- (4) Hay, J. C. SNARE complex structure and function. *Exp. Cell Res.* **2001**, *271*, 10–21.
- (5) Ungar, D.; Hughson, F. M. SNARE protein structure and function. *Annu. Rev. Cell Dev. Biol.* **2003**, *19*, 493–517.
- (6) Weber, T.; Zemelman, B. V.; McNew, J. A.; Westermann, B.; Gmachl, M.; Parlati, F.; Sollner, T. H.; Rothman, J. E. SNAREpins: minimal machinery for membrane fusion. *Cell* **1998**, *92*, 759–772.
- (7) Weimbs, T.; Low, S. H.; Chapin, S. J.; Mostov, K. E.; Bucher, P.; Hofmann, K. A conserved domain is present in different families of vesicular fusion proteins: a new superfamily. *Proc. Natl. Acad. Sci. U. S. A.* **1997**, *94*, 3046–3051.
- (8) Fasshauer, D.; Eliason, W. K.; Brunger, A. T.; Jahn, R. Identification of a minimal core of the synaptic SNARE complex sufficient for reversible assembly and disassembly. *Biochemistry* **1998**, *37*, 10354–10362.
- (9) Dietrich, L. E.; Boeddinghaus, C.; LaGrassa, T. J.; Ungeremann, C. Control of eukaryotic membrane fusion by N-terminal domains of SNARE proteins. *Biochim. Biophys. Acta* **2003**, *1641*, 111–119.
- (10) Fernandez, I.; Ubach, J.; Dulubova, I.; Zhang, X.; Sudhof, T. C.; Rizo, J. Three-dimensional structure of an evolutionarily conserved N-terminal domain of syntaxin 1A. *Cell* **1998**, *94*, 841–849.
- (11) Nicholson, K. L.; Munson, M.; Miller, R. B.; Filip, T. J.; Fairman, R.; Hughson, F. M. Regulation of SNARE complex assembly by an N-terminal domain of the t-SNARE Sso1p. *Nat. Struct. Biol.* **1998**, *5*, 793–802.
- (12) Dulubova, I.; Yamaguchi, T.; Wang, Y.; Sudhof, T. C.; Rizo, J. Vam3p structure reveals conserved and divergent properties of syntaxins. *Nat. Struct. Biol.* **2001**, *8*, 258–264.
- (13) Antonin, W.; Dulubova, I.; Arac, D.; Pabst, S.; Plitzner, J.; Rizo, J.; Jahn, R. The N-terminal domains of syntaxin 7 and vti1b form three-helix bundles that differ in their ability to regulate SNARE complex assembly. *J. Biol. Chem.* **2002**, *277*, 36449–36456.
- (14) Filippini, F.; Rossi, V.; Galli, T.; Budillon, A.; D'Urso, M.; D'Esposito, M. Longins: a new evolutionary conserved VAMP family sharing a novel SNARE domain. *Trends Biochem. Sci.* **2001**, *26*, 407–409.
- (15) Gonzalez, L. C., Jr.; Weis, W. I.; Scheller, R. H. A novel snare N-terminal domain revealed by the crystal structure of Sec22b. *J. Biol. Chem.* **2001**, *276*, 24203–24211.
- (16) Tochio, H.; Tsui, M. M.; Banfield, D. K.; Zhang, M. An autoinhibitory mechanism for nonsyntaxin SNARE proteins revealed by the structure of Ykt6p. *Science* **2001**, *293*, 698–702.
- (17) McNew, J. A.; Sogaard, M.; Lampen, N. M.; Machida, S.; Ye, R. R.; Lacomis, L.; Tempst, P.; Rothman, J. E.; Sollner, T. H. Ykt6p, a prenylated SNARE essential for endoplasmic reticulum-Golgi transport. *J. Biol. Chem.* **1997**, *272*, 17776–17783.
- (18) Zhang, T.; Hong, W. Ykt6 forms a SNARE complex with syntaxin 5, GS28, and Bet1 and participates in a late stage in endoplasmic reticulum-Golgi transport. *J. Biol. Chem.* **2001**, *276*, 27480–27487.
- (19) Dilcher, M.; Kohler, B.; von Mollard, G. F. Genetic interactions with the yeast Q-SNARE VTI1 reveal novel functions for the R-SNARE YKT6. *J. Biol. Chem.* **2001**, *276*, 34537–34544.
- (20) Hasegawa, H.; Zinsser, S.; Rhee, Y.; Vik-Mo, E. O.; Davanger, S.; Hay, J. C. Mammalian ykt6 is a neuronal SNARE targeted to a specialized compartment by its profilin-like amino terminal domain. *Mol. Biol. Cell* **2003**, *14*, 698–720.
- (21) Fukasawa, M.; Varlamov, O.; Eng, W. S.; Sollner, T. H.; Rothman, J. E. Localization and activity of the SNARE Ykt6 determined by its regulatory domain and palmitoylation. *Proc. Natl. Acad. Sci. U. S. A.* **2004**, *101*, 4815–4820.
- (22) Wen, W.; Yu, J.; Pan, L.; Wei, Z.; Weng, J.; Wang, W.; Ong, Y. S.; Tran, T. H.; Hong, W.; Zhang, M. Lipid-Induced conformational switch controls fusion activity of longin domain SNARE Ykt6. *Mol. Cell* **2010**, *37*, 383–395.
- (23) Harvey, M. J.; Giupponi, G.; De Fabritiis, G. ACEMD: accelerating biomolecular dynamics in the microsecond time scale. *J. Chem. Theory Comput.* **2009**, *5*, 1632–1639.
- (24) Brooks, B. R.; Brooks, C. L.; Mackerell, A. D.; Nilsson, L.; Petrella, R. J.; Roux, B.; Won, Y.; Archontis, G.; Bartels, C.; Boresch, S.; Caflisch, A.; Caves, L.; Cui, Q.; Dinner, A. R.; Feig, M.; Fischer, S.; Gao, J.; Hodoscek, M.; Im, W.; Kuczera, K.; et al. CHARMM: the biomolecular simulation program. *J. Comput. Chem.* **2009**, *30*, 1545–1614.
- (25) Sapay, N.; Tieleman, D. P. Combination of the CHARMM27 force field with united-atom lipid force fields. *J. Comput. Chem.* **2011**, *32*, 1400–1410.
- (26) Jorgensen, W. L.; Chandrasekhar, J.; Madura, J. D.; Impey, R. W.; Klein, M. L. Comparison of simple potential functions for simulating liquid water. *J. Chem. Phys.* **1983**, *79*, 926–935.
- (27) Dominguez, C.; Boelens, R.; Bonvin, A. M. J. J. HADDOCK: A protein-protein docking approach based on biochemical or biophysical information. *J. Am. Chem. Soc.* **2003**, *125*, 1731–1737.
- (28) De Vries, S. J.; van Dijk, A. D. J.; Krzeminski, M.; van Dijk, M.; Thureau, A.; Hsu, V.; Wassenaar, T.; Bonvin, A. M. J. J. HADDOCK versus HADDOCK: New features and performance of HADDOCK2.0 on the CAPRI targets. *Proteins* **2007**, *69*, 726–733.
- (29) Feenstra, K. A.; Hess, B.; Berendsen, H. J. C. Improving efficiency of large time-scale molecular dynamics simulations of hydrogen-rich systems. *J. Comput. Chem.* **1999**, *20*, 786–798.
- (30) Darden, T.; York, D.; Pedersen, L. Partical Mesh Ewald - an n.log(n) method for ewald sums in large systems. *J. Chem. Phys.* **1993**, *98*, 10089–10092.
- (31) Humphrey, W.; Dalke, A.; Schulten, K. VMD: Visual molecular dynamics. *J. Mol. Graph. Model.* **1996**, *14*, 33–38.
- (32) Heyer, L. J.; Kruglyak, S.; Yoosheph, S. Exploring expression data: identification and analysis of coexpressed genes. *Genome Res.* **1999**, *9*, 1106–1115.
- (33) Phillips, J. C.; Braun, R.; Wang, W.; Gumbart, J.; Tajkhorshid, E.; Villa, E.; Chipot, C.; Skeel, R. D.; Kale, L.; Schulten, K. Scalable molecular dynamics with NAMD. *J. Comput. Chem.* **2005**, *26*, 1781–1802.

- (34) Hasegawa, H.; Yang, Z.; Oltedal, L.; Davanger, S.; Hay, J. C. Intramolecular protein-protein and protein-lipid interactions control the conformation and subcellular targeting of neuronal Ykt6. *J. Cell Sci.* **2004**, *117*, 4495–4508.